Journal Name

ARTICLE

Vertically Aligned Ultrathin SnS_2 Nanosheets with Strong Photon Capturing Capability for Efficient Photoelectrochemical Water Splitting

Received 00th January 20xx,
Accepted 00th January 20xx

DOI: 10.1039/x0xx00000x

www.rsc.org/

Guangbo Liu[a, c‡], Zhonghua Li[a‡], Tawfique Hasan[b‡], Xiaoshuang Chen[a], Wei Zheng[a], Wei Feng[a], Dechang Jia[d], Yu Zhou[d], PingAn Hu[a]*

Two-dimensional (2D) metal dichalcogenides have emerged as attractive materials for application in photoelectrochemical (PEC) water splitting due to their unique structure and strong interaction with light. To date, deposition of exfoliated 2D nanosheet dispersions onto conductive substrates by a variety of techniques (e.g. casting, spin-coating and self-assembly) is the mostly exploited approach to fabricate photoelectrodes from these materials. However, such solution processing strategies do not allow for control over flake orientation and formation of intimate electrical contacts with the conductive substrates. This could negatively affect the PEC efficiency. Herein, we demonstrate, for the first time, vertically aligned 2D SnS_2 nanosheets with controllable growth and density on conductive substrates (FTO and carbon cloth (CC)) by a modified chemical vapor deposition (CVD) method. In PEC measurements, these vertically aligned 2D SnS_2 nanosheet photoelectrodes exhibit incident a high photon to current conversion efficiency (IPCE) of up to 40.57% for SnS_2⊥CC and 36.76% for SnS_2⊥FTO at 360 nm, and a high photocurrent density of up to 1.92±0.01 mA/cm^2 for SnS_2⊥CC and 1.73±0.01 mA/cm^2 for SnS_2⊥FTO at 1.4 V vs. reversible hydrogen electrode (RHE). These values are two times higher than that of their photoelectrode (SnS_2//FTO) counterparts prepared by conventional spin-coating. Our demonstration of this controllable growth strategy offers a versatile framework towards to design and fabrication of high performance PEC photoelectrodes based on 2D metal chalcogenides.

1. Introduction

Photoelectrochemical (PEC) water splitting, mimicking natural photosynthesis process in plants that produces clean hydrogen fuel, has been widely recognized as a promising strategy for renewable solar energy harvesting and storage in the past decade.[1] This technique integrates solar energy collection together with water electrolyser systems. Like water electrolysers, a PEC water-splitting device requires a catalyst to improve the reaction kinetics and decrease the overpotential for the hydrogen evolution reaction (HER) or oxygen evolution reaction (OER) at the electrodes.[2] Platinum (Pt) and certain precious metal oxide are efficient catalysts for this. However their high cost and scarcity restrict their adoption in commercial-scale solar water splitting.[3] To find earth abundant alternatives, numerous efforts have been focused on nanostructured semiconductors in the past decade.[4, 5] Even for the case of bulks materials with low activity, high surface area of corresponding nanostructures have been demonstrated to allow for possible realization of efficient solar energy conversion by increasing photon collection and lowering minority carrier recombination.[6]

Among these nanostructures, two-dimensional (2D) graphene-like layered crystals (e.g. MoS_2, WSe_2 and SnS_2) have recently emerged as attractive candidates for low cost catalytic materials for solar water splitting.[6-10] These semiconducting 2D layered crystals exhibit tunable bandgap in the range of 1.07~2.44 eV depending on the number of atomic layers, enabling them absorb a large part of the solar spectrum.[6, 7] In addition, 2D sheets show stronger capability of sunlight capturing than common semiconductors (Si and GaAs), achieving up to 10% absorption of incident solar irradiation for < 1 nm thickness.[11, 12] Pioneering investigations using 2D sheets of WS_2 and SnS_2 as photocatalyst in PEC solar water splitting have been demonstrated recently.[8, 10] However, these photoelectrodes were fabricated by deposition of exfoliated 2D sheets (WS_2, SnS_2) onto conductive substrates. This solution processed fabrication approach has several inherent drawbacks for PEC water splitting. First, inevitable agglomeration and re-stacking during electrode fabrication decrease the effective area for photon capturing. This also impedes the direct pathways for charge

[a] Key Laboratory of Micro-systems and Micro-structures Manufacturing of Ministry of Education, Harbin Institute of Technology, Harbin 150080, P. R. China. *E-mail: hupa@hit.edu.cn*
[b] *Cambridge Graphene Centre, University of Cambridge, Cambridge, CB3 0FA, UK.*
[c] School of Chemistry and Chemical Engineering, Harbin Institute of Technology, Harbin, 150001, P. R. China.
[d] *Institute for Advanced Ceramics, Harbin Institute of Technology, Harbin 150001, China*

†Electronic Supplementary Information (ESI) available: The experimental details, supporting figures and additional data. See DOI: 10.1039/x0xx00000x

‡ These authors contributed equally to this work.

transfer, which may increase the probability for charge recombination;[6, 13] Second, good ohmic contact between the conductive substrate and the deposited 2D sheet-based film is not easily established, hindering the rapid transport of electrons, and thus, increasing the carrier recombination.[9, 10]

To exploit the advantages of the 2D nanosheets while avoiding the abovementioned limitations, an ideal architecture of nanostructured film could be envisaged, composed of vertically oriented 2D sheet array with high crystallinity and good electrical contact with the conductive substrate (Scheme 1). This could allow effective harvesting of the photons and photocurrent, aided by strong light absorption, short minority-carrier transport distances and large exposed surface area for the catalytic reactions.[6] Indeed, architectures composed of nanostructured designs based on silicon pillar array,[14] vertically aligned tantalum nitride (Ta_3N_3) nanorods[15] and aligned nanosheets of WO_3,[16, 17] Bi_2WO_6,[18] and $BiVO_4$[19] have been realized for similar applications. However, controllable growth of vertically oriented graphene-like layered metal dichalcogenide arrays (such as of SnS_2) with desired morphology and their application in PEC water splitting have not been demonstrated yet due to the lack of effective synthesis techniques.

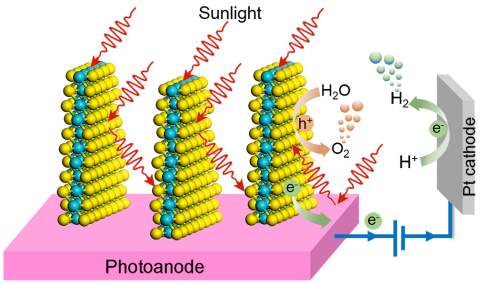

Scheme 1 Schematic illustration to demonstrate the efficient photon capturing and charge transport in vertically aligned 2D SnS_2 nanosheets based photoelectrode.

Here, we demonstrate direct synthesis of wafer-scale vertically aligned 2D SnS_2 nanosheets with different coverage density on to conductive substrates (FTO and CC) using an improved CVD method. The density of the 2D SnS_2 nanosheets can be controlled by reaction temperature. The as-obtained vertical 2D SnS_2 arrays exhibit mono-dispersive and/or highly-compact and open morphology, with well-defined structures and maximally exposed surfaces/edges. The resulting vertically aligned nanosheet-based photoelectrodes show an IPCE value as high as 40.57% for $SnS_2 \perp$CC and 36.76% for $SnS_2 \perp$FTO at 360 nm. The photocurrent density achieved for $SnS_2 \perp$CC and $SnS_2 \perp$FTO photoelectrodes is up to 1.92 $\pm$ 0.01 mA/cm^2 and 1.73 $\pm$ 0.01 mA/cm^2 at 1.4 V vs. RHE, respectively. These values are much higher than that of their parallel counterpart photoelectrode (SnS_2//FTO) prepared by conventional spin-coating.

2. Results and discussion

2.1 Synthesis and morphology characterizations.

Like many other 2D-layered metal dichalcogenides, SnS_2 crystals tend to grow parallel to the substrate during CVD process.[20-22] We realize the growth of vertical SnS_2 nanosheet arrays on conductive substrates (FTO and CC) via an improved CVD method (Fig. 1a) under low temperature. We find that the growth orientation and morphologies of 2D SnS_2 can be controlled at low growth temperature (450°C) by using low boiling point stannic chloride ($SnCl_4 \bullet 5H_2O$). Such control over growth cannot be achieved by using typical high boiling point precursors (e.g. Sn and SnO_2) which require CVD at higher growth temperatures (>680°C).[20-24] The vertical SnS_2 nanosheet arrays can be grown onto planar FTO and curved carbon cloth using our improved CVD method (Fig. 1b).

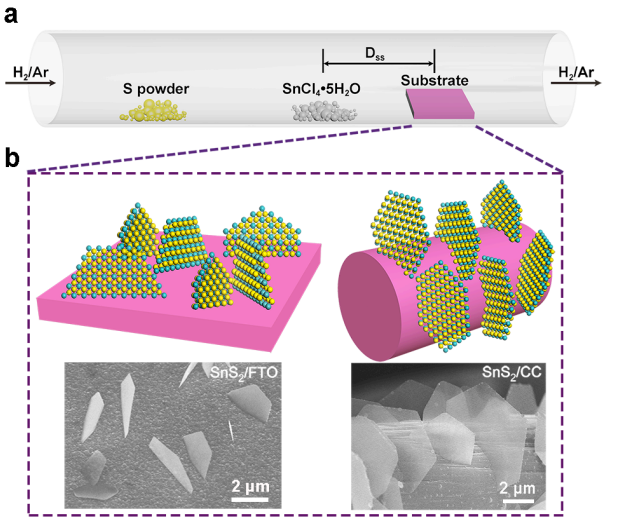

Fig. 1 Schematic illustration for the design and synthesis of vertically aligned 2D SnS_2 nanosheets. (a) Schematic for CVD growth. (b) Morphological models and SEM images of vertically aligned 2D SnS_2 nanosheets grown on planar/curved substrates.

We next control the coverage of the SnS_2 nanosheets on the substrates at different reaction temperature by adjusting the distance between the Sn source and growth substrate (D_{ss}). To achieve this, a series of growth substrates (FTO and CC) are placed downstream to the Sn source center at D_{ss} = 3, 8 and 11 cm. These three D_{ss} locations correspond to 441±1°C, 404±1°C and 337±1°C growth temperature, respectively (see Fig. S1, ESI†). Fig. 2a and b show photographs of the vertically aligned 2D SnS_2 nanosheets grown on FTO (a) and CC (b). The transparency and color evolution of the as-grown SnS_2 nanosheets on FTO substrates obtained at different D_{ss} locations are obvious. As shown in Fig. 2a, the bare FTO becomes less transparent with a light dull yellow hue with D_{ss} = 3 cm (441±1°C). This turns to a deep yellow color with D_{ss} = 8 cm (404±1°C); and becomes virtually opaque with significantly deeper yellow color for D_{ss} =11 cm (337±1°C). These color changes are attributed to the level of coverage of SnS_2 nanosheets on FTO substrates grown at different temperatures (441±1°C, 404±1°C and 337±1°C). Similar color evolution and nanostructure are also observed from SnS_2 nanosheets grown on CC in identical growth conditions (Fig. 2b).

Scanning electron microscopy (SEM) is used to characterize the coverage and morphology of the SnS_2 nanosheets grown on FTO and CC substrates under different growth D_{ss}. For D_{ss}=3 cm (441±1°C), monodispersed SnS_2 nanosheets are vertically grown

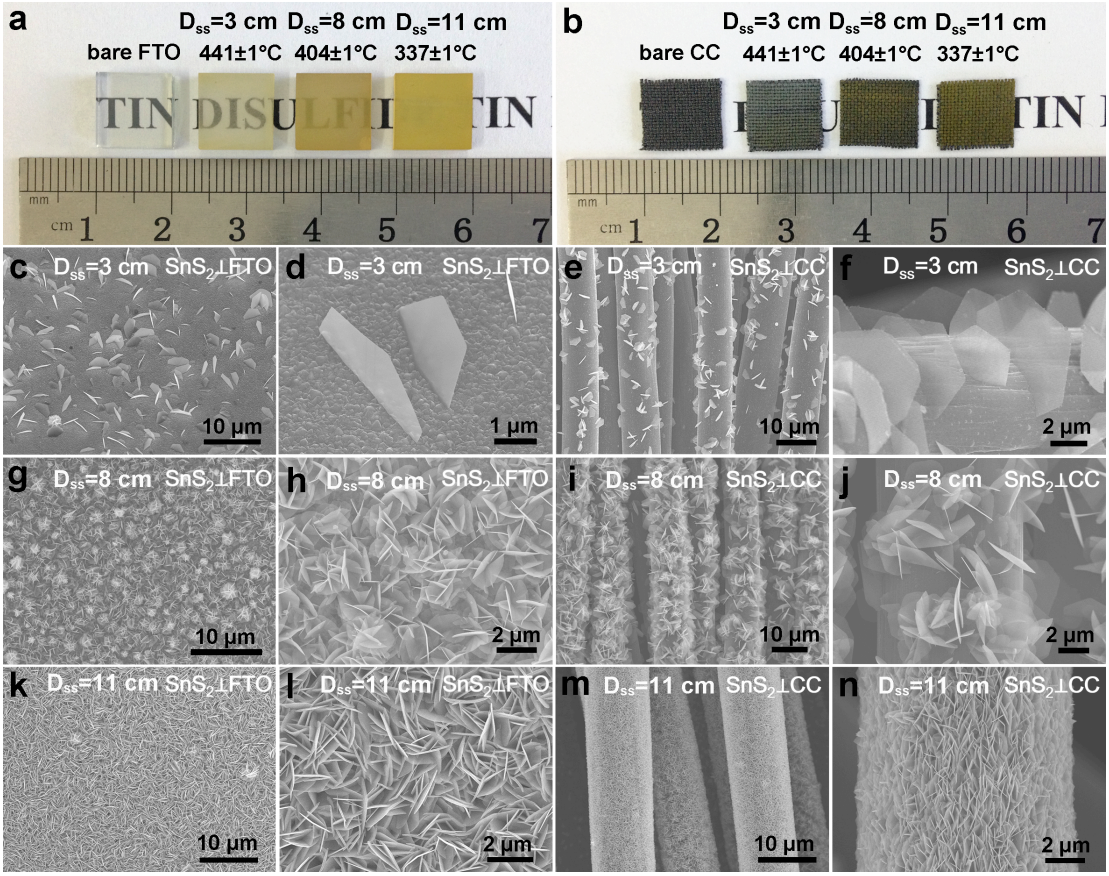

Fig. 2 Morphology characterizations of vertically aligned 2D SnS2 nanosheets as a function of growth temperature. (a) Photographs and (c, d, g, h, k, l) SEM images of vertically aligned 2D SnS2 nanosheets grown on FTO substrate. (b) Photograph and (e, f, i, j, m, n) SEM images of vertically aligned 2D SnS_2 nanosheets grown on CC

onto both FTO and CC substrates. These SnS_2 nanosheets, displaying an open morphology with well-defined structures have a lateral size of 3-10 μm and a thickness of 10~30 nm (Fig. 2c-f). Moreover, the nanosheets grown on FTO always show a well-defined semi-hexagonal shape with three or four crystal edges (Fig. 2d). Crystals with similar morphologies are formed on CC substrates together with well-defined sub-hexagonal shapes having five crystal edges (Fig. 2f). As shown in Fig. 2g-j, with D_{ss}= 8 cm (404±1°C), the SnS_2 nanosheets still grow vertically with a lateral size of 2-5 μm and a thickness of 10-30 nm, with much increased coverage. Furthermore, for D_{ss} = 11 cm (337±1°C) as shown in Fig. 2k-n, full coverage of vertical SnS_2 nanosheets with a lateral size of 1-3 μm and thickness of 20-50 nm are obtained on both planar FTO and curved fibers in CC substrates. This vertically aligned morphology observed in both these substrates is strongly desired since it enables a higher density of SnS_2 nanosheets with highly exposed surface area and edges per unit area of a substrate. This is conducive to achieving a high PEC performance.[25, 26]

2.2 Crystallographic and microstructure characterizations.

X-ray diffraction (XRD) is used to study the crystallographic structure of the as-grown SnS_2 nanosheets on both FTO and CC substrates (Fig. 3a). Disregarding the peaks from the substrates, the diffraction peaks in the XRD spectra of SnS_2 nanosheets on both substrates match well with the hexagonal structure of 2H-SnS_2 (JCPDS No. 89-2358). The XRD pattern of the SnS_2 nanosheets on FTO substrate show six diffraction peaks, corresponding with (001), (100), (011), (012), (110) and (111) facets. In addition to the above six diffraction peaks, the XRD pattern obtained from SnS_2 nanosheets on CC shows two new diffraction peaks of (003) and (103) facets. These are likely from the disorder and random growth orientation on the curved substrate surface.

The as-grown SnS_2 nanosheets are further characterized by transmission electron microscope (TEM). Fig. 3b shows a typical low-magnification TEM image of a planar SnS_2 nanosheet that has a well-defined semi-hexagonal shape. Fig. 3c and d respectively demonstrate elemental mapping images of Sn and S atoms from the red-boxed region in Fig. 3b using energy dispersive X-ray spectroscopy (EDS). These elemental mapping images confirm homogeneous distribution of elemental Sn and S in the nanosheets with an elemental ratio of ~1:2 (Fig. S2, ESI†). The high-resolution TEM (HRTEM) image in Fig. 3e is obtained from the corresponding green-boxed region in Fig. 3b with the selected area electron diffraction (SAED) pattern as an inset. This SAED is a single set of perfect hexagonal pattern, indicating that the SnS_2 nanosheet is of single-crystal quality with expected hexagonal crystal structure. The crystal planes labeled in the SAED pattern is the (100) plane, and the angles between them are ~120°. Therefore, the mainly exposed surfaces of SnS_2 nanosheets are (001) basal planes. This agrees well with the XRD patterns that exhibit the highest strength at (001) peak. The interplanar lattice spacing is ~3.15 Å (Fig. 3e),

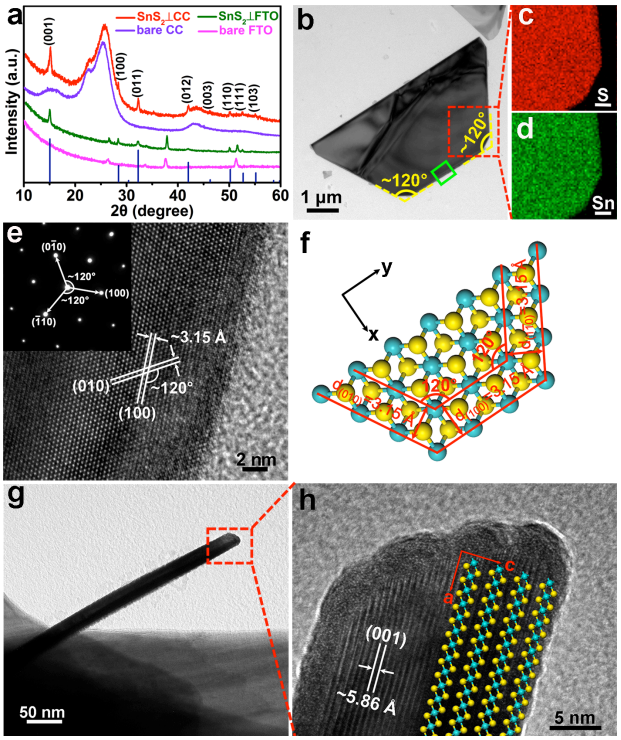

Fig. 3 Crystallographic and microstructural characterizations of as-grown 2D SnS_2 nanosheets. (a) XRD patterns of the vertical SnS_2 nanosheets grown on FTO and CC. (b) Low-magnification TEM image of a planar SnS_2 nanosheet, and elemental mapping images of (c) S and (d) Sn taken from the red boxed region shown in (b). Scale bars are 200 nm. (e) High-resolution TEM (HRTEM) image taken from the green boxed region in (b) and corresponding SAED pattern (inset). (f) Crystal structure model of (b) shows the crystallographic information. (g) Low-magnification TEM image of a SnS_2 nanosheet across its thickness. (h) HRTEM image presents laminar structures with an inter-planar distance of ~5.86 Å.

corresponding to the (100) planes of SnS_2. The intersection angle between them is ~120°, consistent with the angle values measured in SAED pattern. These results agree well with the previously reported lattice parameters for SnS_2 crystals prepared via CVD methods.[20, 22, 24, 27] Based on the above analysis, a semi-hexagonal 2D crystal structure model presenting the crystallographic structure of the as-grown SnS_2 nanosheets is provided in Fig. 3f. As seen that the exposed facets of the semi-hexagonal shaped vertical SnS_2 nanosheet are the (100), (010) and $(1\bar{1}0)$ planes, implying that these are the mostly developed planes during the crystal growth. Fig. 3g presents the top-view TEM image of one ~18 nm thick SnS_2 nanosheet with a lamellar structure. It has a lattice spacing of 5.86 Å, corresponding to the (001) interplanar distance of hexagonal SnS_2 (shown in HRTEM image of Fig. 3h).

2.3 Growth mechanism of the vertical 2D SnS_2 nanosheets.

Based on the above crystallographic and microstructure analyses, we now propose a possible growth mechanism of our vertically aligned 2D SnS_2 nanosheets. For some wet-chemical-based methods, the formation of the 2D SnS_2 nanosheets is attributed to the adsorption of certain growth inhibitors (chemical additives such as molecular precursors and organic/non-aqueous solvents) on the (001) facet during the growth process. These suppress the crystal growth along the [001] direction, leading to 2D structures.[28-30] For our CVD growth process, however, no equivalent growth inhibitors confine the growth of the (001) atomic planes to promote the formation of 2D SnS_2. This is because impurities that could act as growth inhibitors are not detected in the SnS_2 crystal domains by EDS (Fig. 3c, d and Fig. S2, ESI†). Therefore, the growth of our 2D SnS_2 nanosheets is controlled by their intrinsic properties, which is described in Fig. 4. As shown in Fig. 4a, SnS_2 has a hexagonal CdI_2-type crystal layered structure, in which the Sn and S atoms are covalently bound together on the layers, while the adjacent layers are coupled by weak van der Waals forces.[8, 31, 32] Based on this anisotropic atomic bonding feature of SnS_2 (Fig. 4a), it is expected that the surface energy along [100] and [010] is much higher than that along [001].[33] The surface energies (γ) of {100} and {001} planes are 0.034 and 0.0065 eV/Å^2, respectively.[33] Bravais law dictates that the atomic planes with higher surface energy usually exhibit higher growth rates than those with lower surface energy.[26] Therefore, as illustrated in Fig. 4b, once the SnS_2 nuclei forms on the substrate surface, the new SnS_2 species arriving preferentially incorporate themselves into the crystal lattice along the {100} planes rather than the {001} planes because of the much higher surface energy along [100] and [010] than that along [001].[26, 30, 34] Consequently, such anisotropy results in fast transverse growth and slow longitudinal growth in {001} planes. This makes the {001} planes develop into the most exposed basal planes, forming the 2D SnS_2 structure.[34] Additionally, there are small differences between the SnS_2 growth on FTO and CC substrates. As illustrated in Fig. 4b, the SnS_2 nanosheets grown on CC can generate further well-defined sub-hexagonal shape with five crystal edges. This is mainly due to the curved surface of the CC substrate fibers, leading to more orientation spaces to develop the intrinsic hexagonal configurations.

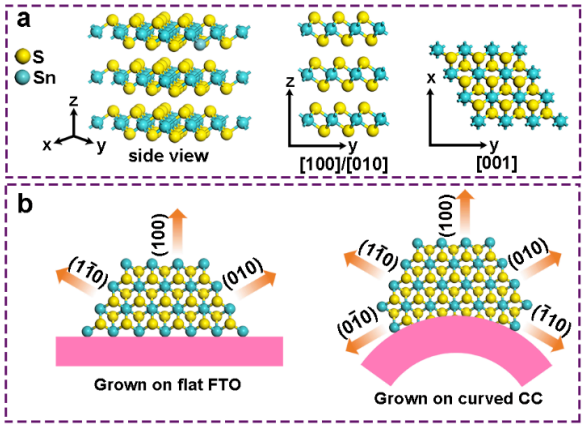

Fig. 4 Schematic illustration of 3D crystal structure and growth mechanism of vertically aligned 2D SnS_2 nanosheets. (a) 3D crystal model of hexagonal SnS_2 view along different directions. (b) Growth process of vertically aligned 2D SnS_2 nanosheets on planar FTO substrate and curved CC surface.

2.4 Photoelectrochemical performances.

To demonstrate the enhancement of light absorption by the vertical SnS_2 architecture, comparative UV-visible extinction measurements are carried out on the as-prepared vertical 2D SnS_2 nanosheet

arrays (SnS_2⊥FTO) and their spin-coated counterpart where the flakes are parallel to the substrate (SnS_2//FTO, see Fig. S3, ESI†). As shown in Fig. 5a, the photo-absorption intensity of SnS_2⊥FTO is significantly increased over the entire visible spectrum as their distribution on FTO substrate increases from monodispersion to full coverage. Compared to the SnS_2//FTO with the similar deposition amount (0.25-0.30 mg/cm^2), the SnS_2⊥FTO with full coverage shows much stronger light absorption due to its highly-compact and vertical morphology through increased light reflection and scattering at the nanosheets interface.[6] The optical band gaps (E_g) of the sample are estimated from the absorption spectra by using the relation:[30, 35]

$$\alpha h\nu = A(h\nu - E_g)^{n/2} \quad (1)$$

where α, h, ν, A and E_g are the absorption coefficient, Planck's constant, light frequency, proportionality constant and optical band gap of the materials, respectively. In above relation, n = 4 for indirect band gap semiconductor, such as SnS_2. By extrapolating the linear part of the transformed $(\alpha h\nu)^2$ vs. photon energy plots in Fig. 5b, the E_g values are calculated in the range of 2.18-2.25 eV for both of the SnS_2⊥FTO and SnS_2//FTO. These values agree well with the previous reports on nanostructured SnS_2 (2.18-2.44 eV).[8, 30, 36-38] This improved photo-absorption implies that the vertically oriented SnS_2 nanostructured architectures have a stronger capability for photon capturing than their parallel counterpart.

The photoelectrochemical water splitting properties of the vertical 2D SnS_2 nanosheet arrays are investigated by using different coverage samples on both FTO and CC (SnS_2⊥FTO and SnS_2 ⊥ CC), as well as their parallel counterpart (SnS_2//FTO). The measurements are performed in 0.5 M Na_2SO_4 electrolyte using a three-electrode setup under simulated solar light illumination. As shown in Fig. 5c, the photocurrents generated from both of the SnS_2⊥FTO and SnS_2⊥CC photoanodes are highly increased as their distribution increases from monodispersion to full coverage on the substrates. At 1.4 V vs. RHE under AM 1.5 G 100 mW/cm^2 solar light, the photocurrent density values are below 0.1 mA/cm^2 for both of the SnS_2 ⊥ FTO and SnS_2 ⊥ CC photoanodes with monodispersed coverage of vertical 2D SnS_2 nanosheets. These values increase to ~0.6-0.7 mA/cm^2 as the vertical nanosheets reach a relatively high coverage on substrates. For samples with full coverage, the photocurrent density reaches to 1.92±0.01 mA/cm^2 for SnS_2⊥CC photoanode and 1.73±0.01 mA/cm^2 for SnS_2⊥FTO photoanode. In contrast, the SnS_2//FTO photoanode with similar material deposited on substrates shows a photocurrent density of 0.91±0.01 mA/cm^2. This is only about half of those of the vertical counterpart photoanodes with full coverage, confirming the much efficient PEC water splitting properties of the vertically aligned 2D SnS_2 nanosheet arrays. Fig. 5d shows the time-dependent current change curves of SnS_2⊥FTO, SnS_2⊥CC and SnS_2//FTO photoanodes measured at a bias potential of 1.2 V vs. RHE under AM 1.5 G 100 mW/cm^2 solar light. All the SnS_2⊥FTO and SnS_2⊥CC photoanodes demonstrate good stability during the two-minute test. We propose this is because the as-grown vertical SnS_2 nanosheets form a good interface with the conductive substrate. However, the SnS_2//FTO photoanode reveals an apparent decline in its time-dependent current change curve. This is likely due to sample shedding during the test due to the weak interacial adhesion between the spin-coated SnS_2 nanosheets and the FTO substrate.

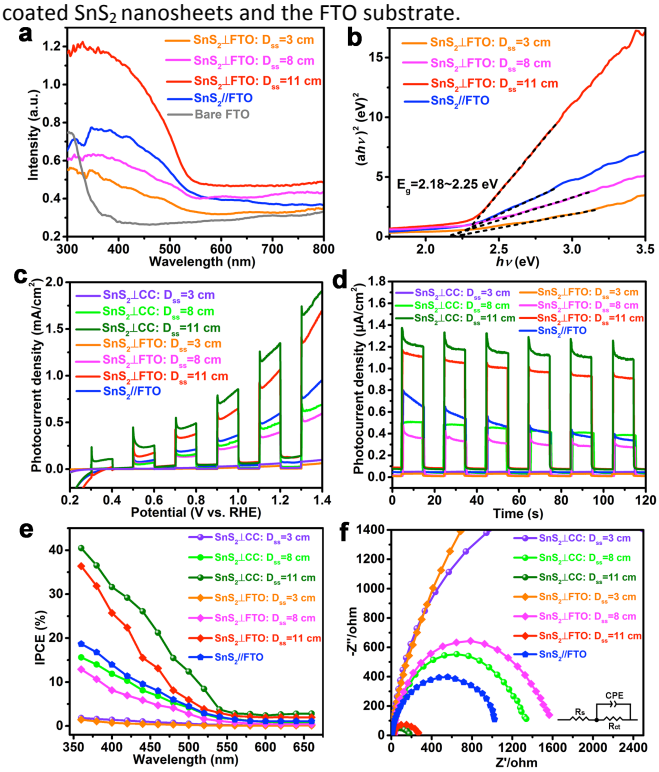

Fig. 5 Photoelectrochemical properties of the as-grown vertically aligned SnS_2 nanosheets and parallel SnS_2 nanosheets. (a) UV-visible absorption spectra and (b) corresponding Tauc plots of SnS_2 nanosheets and parallel SnS_2 nanosheets on FTO substrates. (c) Photocurrent density curves of SnS_2 nanosheets and parallel SnS_2 nanosheets. (d) Photoelectrochemical response curves of SnS_2 nanosheets and parallel SnS_2 nanosheets. (e) IPCE spectra of the vertical SnS_2 nanosheets and parallel SnS_2 nanosheets. (f) Electrochemical impedance spectra measured at 1.2 V vs. RHE.

To characterize the photoconversion efficiency of the SnS_2⊥FTO, SnS_2 ⊥ CC and SnS_2//FTO photoanodes, photocurrent generation is measured under monochromatic light illumination and plotted as a function of wavelength (Fig. 5e). The IPCE is calculated using the equation:[39]

$$\text{IPCE} = (1240 I_{ph})/(p\lambda) \quad (2)$$

where I_{ph} is the measured photocurrent density (μA/cm^2) at a specific wavelength λ (nm) of the incident monochromatic light and p is the incident power intensity (μW/cm^2). As shown in Fig. 5e, the SnS_2⊥FTO and SnS_2⊥CC photoanodes exhibit significantly enhanced IPCE over the entire visible spectrum as their distribution on the substrates from monodispersion to full coverage. Under 360 nm, the IPCE values are only 2-3% for SnS_2 ⊥ FTO and SnS_2 ⊥ CC photoanodes with monodispersion coverage. These values increase to 13-16% for photoanodes with increased coverage. As for the photoanodes with full coverage, however, the highest IPCE values achieved are up to 40.57% for SnS_2⊥FTO photoanode and 36.76% for SnS_2⊥CC photoanode at 360 nm. These values are much higher than the 18.68% for their parallel counterpart SnS_2//FTO photoanode. This ultrahigh IPCE implies that the photogenerated

electrons and holes are separated and transported efficiently in the vertical SnS_2 nanosheet structures. We note that the onset of the IPCE is at ~560 nm, corresponding to the band gap energy of 2.21 eV. This agrees well with the measured absorption edge of 2.18-2.25 eV for 2D SnS_2 nanosheets (Fig. 5b).

To better understand the PEC performance, electrochemical impedance spectroscopy (EIS) is used to elucidate the interfacial charge transfer resistance (R_{ct}) of the 2D SnS_2 nanosheet photocathodes (Fig. 5f). The arches for vertical 2D SnS_2 nanosheet-based photocathodes are greatly decreased with their distribution from monodispersion to full coverage on the substrates, implying a much small R_{ct} for full coverage $SnS_2 \perp$ FTO and $SnS_2 \perp$ CC photoanodes. Compared with the $SnS_2 \perp$ FTO and $SnS_2 \perp$ CC photoanodes with full coverage, the SnS_2//FTO photoanode with similar loading amount exhibits much larger R_{ct} due to the significantly high interfacial resistance between parallel SnS_2 nanosheets themselves and with the FTO substrate.

The as-grown vertical 2D SnS_2 nanosheet arrays exhibit excellent PEC performance in visible-light water splitting, showing high IPCE and very large photocurrent density. We compared our performance data of vertical SnS_2 to its spin-coated one and other photocatalyst materials. The performance of vertical SnS_2 is not only significantly superior to their spin-coated photoanode counterparts, but also better than or comparable to those of many other reported solution processed photoelectrodes based on layered metal chalcogenides (Table S1, ESI†). For instance, the IPCE value (40.47% for $SnS_2\perp$CC and 36.76% for $SnS_2\perp$FTO at 360 nm) and photocurrent density (1.92 ± 0.01 mA/cm^2 for $SnS_2\perp$CC and 1.73 ± 0.01 mA/cm^2 for $SnS_2\perp$FTO at 1.4 V vs. RHE) of our vertically aligned SnS_2 nanosheet photoelectrodes are much higher than that of the reported In_2S_3 nanoflake photoelectrodes prepared by spin-coating (photocurrent density ~1.1 mA/cm^2 at 1.3 V vs RHE and IPCE of 2.5% at 300 nm);[40] and is also comparable to the IPCE value of 38.7% at 420 nm and photocurrent density of 2.75 mA/cm^2 at 1.0 V vs. Ag/AgCl for freestanding SnS_2 single-layer nanosheets.[8] To be pointed out, the obtained performance data are depended on the measurement conditions (e.g. PH value and type of the electrolyte, amount of the catalyst). This high PEC performance is mainly attributed to the vertically aligned architecture as well as intimate contact towards the conductive substrate. On one hand, this vertical architecture enables efficient photon absorption, as evidenced by their UV-visible absorption spectra in Fig. 5a. On the other hand, the good electrical contact with the substrate and highly crystalline nanosheets results in good conducting channels for rapid electron-hole separation and charge migration. Moreover, this vertical 2D SnS_2 nanosheets array with an open morphology exhibits maximally exposed surfaces/edges that can provide high interfacial contact area with the electrolyte for fast interfacial charge migration and surface redox reactions, improving the PEC performance.[6, 8]

3. Conclusions

To summarize, by using bottom-up CVD method, we have successfully synthesized large scale high quality vertically aligned 2D SnS_2 nanosheets on conductive FTO and CC. The density of the SnS_2 nanosheets can be effectively controlled by the growth temperature. Investigations on the crystal structure and growth mechanism of 2D SnS_2 nanosheets indicate that the anisotropic surface energy plays a key role in the formation of the 2D structures. PEC measurements show that the vertically aligned 2D SnS_2 nanosheets with full coverage exhibit remarkable PEC water splitting performance, with the highest IPCE value of up to 40.57% for $SnS_2\perp$CC photoanode and 36.76% for $SnS_2\perp$FTO photoanode at 360 nm. The highest photocurrent density achieved is 1.92 ± 0.01 mA/cm^2 for $SnS_2\perp$CC photoanode and 1.73 ± 0.01 mA/cm^2 for $SnS_2\perp$FTO photoanode at 1.4 V vs. RHE, significantly surpassing their spin-coated SnS_2//FTO photoanode counterpart. We believe that our approach provides new insights into growth of vertically aligned 2D SnS_2 nanosheets and could be universally applied to other 2D materials for PEC and related devices.

Acknowledgements

This work was financially supported by the National Natural Science Foundation of China (NSFC, No. 61390502, 61172001，21373068) and the National Basic Research Program of China (2013CB632900). T. Hasan acknowledges support from a Royal Academy of Engineering research fellowship (Graphlex).

Notes and references

1 M. Gratzel, *Nature*, 2001, **414**, 338-344.
2 M. G. Walter, E. L. Warren, J. R. McKone, S. W. Boettcher, Q. Mi, E. A. Santori and N. S. Lewis, *Chem Rev*, 2010, **110**, 6446-6473.
3 A. Heller, E. Aharon-Shalom, W. A. Bonner and B. Miller, *J Am Chem Soc*, 1982, **104**, 6942-6948.
4 K.-S. Choi, *J Phys Chem Lett*, 2010, **1**, 2244-2250.
5 J. Sun, D. K. Zhong and D. R. Gamelin, *Energy Environ Sci*, 2010, **3**, 1252-1261.
6 M. Zhou, X. W. Lou and Y. Xie, *Nano Today*, 2013, **8**, 598-618.
7 B. Peng, P. K. Ang and K. P. Loh, *Nano Today*, 2015, **10**, 128-137.
8 Y. Sun, H. Cheng, S. Gao, Z. Sun, Q. Liu, Q. Liu, F. Lei, T. Yao, J. He, S. Wei and Y. Xie, *Angew Chem Int Ed*, 2012, **51**, 8727-8731.
9 L. A. King, W. Zhao, M. Chhowalla, D. J. Riley and G. Eda, *J Mater Chem A*, 2013, **1**, 8935.
10 X. Yu, M. S. Prevot, N. Guijarro and K. Sivula, *Nat Commun*, 2015, **6**, 7596.
11 L. Britnell, R. M. Ribeiro, A. Eckmann, R. Jalil, B. D. Belle, A. Mishchenko, Y. J. Kim, R. V. Gorbachev, T. Georgiou, S. V. Morozov, A. N. Grigorenko, A. K. Geim, C. Casiraghi, A. H. C. Neto and K. S. Novoselov, *Science*, 2013, **340**, 1311-1314.
12 M. Bernardi, M. Palummo and J. C. Grossman, *Nano Lett*, 2013, **13**, 3664-3670.
13 S. Mao, Z. Wen, S. Ci, X. Guo, K. K. Ostrikov and J. Chen, *Small*, 2015, **11**, 414-419.
14 I. Oh, J. Kye and S. Hwang, *Nano Lett*, 2012, **12**, 298-302.
15 Y. Li, T. Takata, D. Cha, K. Takanabe, T. Minegishi, J. Kubota and K. Domen, *Adv Mater*, 2013, **25**, 125-131.
16 J. Su, X. Feng, J. D. Sloppy, L. Guo and C. A. Grimes, *Nano Lett*, 2011, **11**, 203-208.
17 W. Li, P. Da, Y. Zhang, Y. Wang, X. Lin, X. Gong and G. Zheng, *ACS Nano*, 2014, **8**, 11770-11777.
18 M. Zhou, J. Bao, M. Tao, R. Zhu, Y. Zeng, Z. Wei and Y. Xie,

Chem Commun, 2012, **48**, 3439-3441.
19 M. Zhou, J. Bao, W. Bi, Y. Zeng, R. Zhu, M. Tao and Y. Xie, *ChemSusChem*, 2012, **5**, 1420-1425.
20 G. Su, V. G. Hadjiev, P. E. Loya, J. Zhang, S. Lei, S. Maharjan, P. Dong, P. M. Ajayan, J. Lou and H. Peng, *Nano Lett*, 2015, **15**, 506-513.
21 J.-H. Ahn, M.-J. Lee, H. Heo, J. H. Sung, K. Kim, H. Hwang and M.-H. Jo, *Nano Lett*, 2015, **15**, 3703-3708.
22 J. Xia, D. Zhu, L. Wang, B. Huang, X. Huang and X.-M. Meng, *Adv Funct Mater*, 2015, **25**, 4255-4261.
23 X. Zhou, Q. Zhang, L. Gan, H. Li, J. Xiong and T. Zhai, *Adv Sci*, 2016, 1600177.
24 X. Zhou, Q. Zhang, L. Gan, H. Li and T. Zhai, *Adv Funct Mater*, 2016, **26**, 4405.
25 Z. Bo, Y. Yang, J. Chen, K. Yu, J. Yan and K. Cen, *Nanoscale*, 2013, **5**, 5180-5204.
26 X.-H. Ma, K.-H. Cho and Y.-M. Sung, *CrystEngComm*, 2014, **16**, 5080-5086.
27 Y. Huang, H. X. Deng, K. Xu, Z. X. Wang, Q. S. Wang, F. M. Wang, F. Wang, X. Y. Zhan, S. S. Li, J. W. Luo and J. He, *Nanoscale*, 2015, **7**, 14093-14099.
28 J.-w. Seo, J.-t. Jang, S.-w. Park, C. Kim, B. Park and J. Cheon, *Adv Mater*, 2008, **20**, 4269-4273.
29 C. Zhai, N. Du and H. Z. D. Yang, *Chem Commun*, 2011, **47**, 1270-1272.
30 R. Wei, J. Hu, T. Zhou, X. Zhou, J. Liu and J. Li, *Acta Mater*, 2014, **66**, 163-171.
31 R. S. Mitchell, Y. Fujiki and Y. Ishizawa, *Nature*, 1974, **247**, 537-538.
32 S. Mandalidis, J. A. Kalomiros, K. Kambas and A. N. Anagnostopoulos, *J Mater Sci*, 1996, **31**, 5975-5978.
33 M. Li, E. Liu, H. Hu, S. Ouyang, H. Xu and D. Wang, *Int J Photoenergy*, 2014, **2014**, 7.
34 J. Feng, J. Chen, B. Geng, H. Feng, H. Li, D. Yan, R. Zhuo, S. Cheng, Z. Wu and P. Yan, *Appl Phys A*, 2011, **103**, 413-419.
35 A. Hagfeldt and M. Graetzel, *Chem Rev*, 1995, **95**, 49-68.
36 J. Chao, Z. Xie, X. Duan, Y. Dong, Z. Wang, J. Xu, B. Liang, B. Shan, J. Ye, D. Chen and G. Shen, *CrystEngComm*, 2012, **14**, 3163-3168.
37 W. Du, D. Deng, Z. Han, W. Xiao, C. Bian and X. Qian, *CrystEngComm*, 2011, **13**, 2071-2076.
38 Y. C. Zhang, Z. N. Du, S. Y. Li and M. Zhang, *Appl Catal B: environ*, 2010, **95**, 153-159.
39 Z. Yi, J. Ye, N. Kikugawa, T. Kako, S. Ouyang, H. Stuart-Williams, H. Yang, J. Cao, W. Luo, Z. Li, Y. Liu and R. L. Withers, *Nature Mater*, 2010, **9**, 559-564.
40 L. Wang, L. Xia, Y. Wu and Y. Tian, *ACS Sustain Chem Eng*, 2016, **4**, 2606-2614.